

**An energy-based finite-strain model for  
3D heterostructured materials  
and its validation by curvature analysis**

Yiannis Hadjimichael, Christian Merdon, Matthias Liero, Patricio Farrell

submitted: December 11, 2023

Weierstrass Institute  
Mohrenstraße 39  
10117 Berlin  
Germany  
E-Mail: [yiannis.hadjimichael@wias-berlin.de](mailto:yiannis.hadjimichael@wias-berlin.de)  
[christian.merdon@wias-berlin.de](mailto:christian.merdon@wias-berlin.de)  
[matthias.liero@wias-berlin.de](mailto:matthias.liero@wias-berlin.de)  
[patricio.farrell@wias-berlin.de](mailto:patricio.farrell@wias-berlin.de)

No. 3064  
Berlin 2023



---

2020 *Mathematics Subject Classification.* 74B20, 74G65, 74S05.

2010 *Physics and Astronomy Classification Scheme.* 46.25.Cc, 68.65.-k, 62.23.Hj.

*Key words and phrases.* Finite-strain elasticity, energy-based model, heterostructures, bent nanowires, curvature.

This research was supported by the Leibniz competition 2020 (NUMSEMIC, J89/2019). Matthias Liero was partially supported by Deutsche Forschungsgemeinschaft (DFG) via the Priority Program SPP 2256 "Variational Methods for Predicting Complex Phenomena in Engineering Structures and Materials" (project no. 441470105), subproject Mi 459/9-1 "Analysis for thermo-mechanical models with internal variables".

Edited by  
Weierstraß-Institut für Angewandte Analysis und Stochastik (WIAS)  
Leibniz-Institut im Forschungsverbund Berlin e. V.  
Mohrenstraße 39  
10117 Berlin  
Germany

Fax: +49 30 20372-303  
E-Mail: [preprint@wias-berlin.de](mailto:preprint@wias-berlin.de)  
World Wide Web: <http://www.wias-berlin.de/>

# An energy-based finite-strain model for 3D heterostructured materials and its validation by curvature analysis

Yiannis Hadjimichael, Christian Merdon, Matthias Liero, Patricio Farrell

## Abstract

This paper presents a comprehensive study of the intrinsic strain response of 3D heterostructures arising from lattice mismatch. Combining materials with different lattice constants induces strain, leading to the bending of these heterostructures. We propose a model for nonlinear elastic heterostructures such as bimetallic beams or nanowires that takes into account local prestrain within each distinct material region. The resulting system of partial differential equations (PDEs) in Lagrangian coordinates incorporates a nonlinear strain and a linear stress-strain relationship governed by Hooke's law. To validate our model, we apply it to bimetallic beams and hexagonal hetero-nanowires and perform numerical simulations using finite element methods (FEM). Our simulations examine how these structures undergo bending under varying material compositions and cross-sectional geometries. In order to assess the fidelity of the model and the accuracy of simulations, we compare the calculated curvature with analytically derived formulations. We derive these analytical expressions through an energy-based approach as well as a kinetic framework, adeptly accounting for the lattice constant mismatch present at each compound material of the heterostructures. The outcomes of our study yield valuable insights into the behavior of strained bent heterostructures. This is particularly significant as the strain has the potential to influence the electronic band structure, piezoelectricity, and the dynamics of charge carriers.

## 1 Introduction

Within the last few decades the complexity of micro- or even nanoelectronic systems has exploded, comprising many small 3D devices. The electronic properties of these devices can be directly customized via (hyper)elastic strain. An example are partially coated nanowires which due to different lattice constants between GaAs core and partial (In,Al)As stressor bend up to 180 degrees [14]. Such a significant hyperelastic strain strongly impacts the band gap which in turn influences charge carrier transport. Moreover, novel fabrication strategies, inspired by biological processes rely on a 3D self-assembly [11]. Spatial self-assembly that can be performed in parallel and directly on a chip (no placement needed) leads to improved performance, for example due to a continuous curvature within a nanotube [24], and enhances the footprint area on the chip. However, for such shapeable electrical systems the influence of strain on electronic properties needs to be better understood. Hence, solid mathematical models are paramount.

In the present paper, we apply an energy-based finite-strain model introduced in [2] to hyperelastic heterostructured nanomaterials. The model is based on the derivative of an energy

function defined in the undeformed space and it is adjusted to capture large deformations. Such deformations appear in GaAs/(In,Al)As core/stressor nanowires where the lattice mismatch of the consisting materials is between 3% and 7%. The relation between stress and strain is governed by a generic Hooke's law and we employ the St. Venant-Kirchhoff strain formulation [29, 30] since it is commonly used for hyperelastic materials. The St. Venant-Kirchhoff model features a nonlinear strain even if the stress-strain relation is linear. The strain nonlinearity is crucial in fully capturing the dynamics of the system, especially in the presence of large deformations [4].

Other hyperelastic models used to predict nonlinear stress-strain behavior include the Ogden model [21] for rubbers, polymers, and biological tissues. Hyperelasticity is also considered in mechanistic models, for instance the Arruda-Boyce model [1] that describes the behavior of incompressible rubber and other polymeric substances. Finally, a nonlinear stress-strain model by [28] describes neo-Hookean solid materials undergoing large deformations.

The resulting model culminates into the partial differential equation that seeks displacement  $\mathbf{u}$  such that

$$-\operatorname{div}(\det(\mathbf{M})(\mathbf{I} + \nabla \mathbf{u})\mathbf{M}^{-1}\mathbf{S}(\mathbf{u})\mathbf{M}^{-T}) = \mathbf{0}$$

holds in the reference (unbent) configuration. Here  $\mathbf{S}$  denotes the stress tensor, while the spatially dependent matrix  $\mathbf{M}$  characterizes the predeformation that causes intrinsic strain within the material and bends the heterostructure. In order to verify our model for the bimetallic beam case and the more advanced setup of a partially coated hexagonal, we compare the curvature of the bent structure with analytical expressions. On the one hand, we derive the curvature by minimizing the strain energy and on the other hand by a kinetic approach, adapting ideas from Timoshenko [27]. We also show under which conditions these two expressions are equivalent. The proposed analysis is equally important as a reverse engineering tool. With the help of the curvature equation, it is possible to determine the necessary material and geometry parameters to achieve a desired bending angle a priori of any computations. Numerical tests on the bimetallic beam and nanowire confirm the theoretical derivations. Finally, our 3D model and simulation lays the foundation for future investigations where the strain is used as an input to more complex charge transport models. The strain directly impacts the band edges of the semiconductor materials. Therefore, ensuring very good agreement with continuum mechanic theory is of extreme importance.

## 1.1 Outline

The rest of this paper is structured as follows: In Section 2, we introduce the notation and provide a hyperelastic deformation model tailored for heterostructured materials. We present two relevant applications, the bimetallic beam and the partially coated nanowire, in Section 3. Furthermore, in Section 4, we derive analytical formulas for the curvature of bent nanowires and discuss their relation to well-known expressions for bent bimetallic beams. In Section 5, we present FEM simulations demonstrating a good agreement between numerical results and theoretical findings. Finally, we provide concluding remarks in Section 6.

## 2 Hyperelastic deformation models

## 2.1 Notation and constitutive laws

Let  $\bar{\Omega}$  be the closure of an arbitrary bounded, open, and connected set  $\Omega \subset \mathbb{R}^3$ . We call  $\bar{\Omega}$  the *reference (Lagrangian or material) configuration* (i.e., initial volume occupied by a body before it is deformed) and denote with

$$\begin{aligned}\phi &: \bar{\Omega} \rightarrow \mathbb{R}^3, \\ \mathbf{u} &: \bar{\Omega} \rightarrow \mathbb{R}^3\end{aligned}$$

the vector fields of *deformation* and *displacement* of the reference configuration, respectively. Following Ciarlet [4], we assume throughout this paper that both deformation and displacement are sufficiently smooth and orientation-preserving, and the deformation is injective (except possibly on  $\partial\Omega$ ). The deformation is related to the displacement via  $\phi(\mathbf{x}) = \mathbf{x} + \mathbf{u}(\mathbf{x})$ , where  $\mathbf{x} \in \bar{\Omega}$  is a generic *Lagrangian variable* (i.e., material point). The deformed space is defined as  $\bar{\Omega}^\phi := \phi(\bar{\Omega})$ , and  $\mathbf{x}^\phi := \phi(\mathbf{x}) \in \bar{\Omega}^\phi$  is the corresponding *Eulerian variable* (i.e., spatial point).

In the following, we adopt the following notations: Let  $\mathbb{M}^n$  be the set of all real square matrices of order  $n$ ,  $\mathbb{M}_+^n = \{\mathbf{A} \in \mathbb{M}^n : \det(\mathbf{A}) > 0\}$ ,  $\mathbb{S}^n = \{\mathbf{A} \in \mathbb{M}^n : \mathbf{A}^\top = \mathbf{A}\}$ , and  $S_{n-1} = \{\mathbf{n} \in \mathbb{R}^n : |\mathbf{n}| = 1\}$ . We also introduce the deformation gradient  $\mathbf{F} := \nabla\phi$  and its Jacobian  $J := \det(\mathbf{F}) > 0$ . The *total strain* is given by the Green-Lagrange strain tensor (also called Lagrangian finite strain tensor or Green–St-Venant strain tensor)

$$\boldsymbol{\varepsilon}(\mathbf{F}) := \frac{1}{2}(\mathbf{F}^\top \mathbf{F} - \mathbf{I}) = \frac{1}{2}(\nabla\mathbf{u} + \nabla^\top\mathbf{u} + \nabla^\top\mathbf{u}\nabla\mathbf{u}). \quad (1)$$

From the Cauchy theorem [4, Theorem 2.3-1], we know that there exists a symmetric continuously differentiable Cauchy stress tensor  $\mathbf{T}^\phi : \bar{\Omega}^\phi \rightarrow \mathbb{S}^3$  (usually denoted by  $\boldsymbol{\sigma}$ ) such that

$$-\operatorname{div}^\phi(\mathbf{T}^\phi(\mathbf{x}^\phi)) = \mathbf{f}^\phi(\mathbf{x}^\phi), \quad \forall \mathbf{x}^\phi \in \Omega^\phi, \quad (2a)$$

$$\mathbf{T}^\phi(\mathbf{x}^\phi)\mathbf{n}^\phi = \mathbf{g}^\phi(\mathbf{x}^\phi), \quad \forall \mathbf{x}^\phi \in \Gamma^\phi \subseteq \partial\Omega^\phi \text{ and } \forall \mathbf{n}^\phi \in S_2, \quad (2b)$$

$$\mathbf{x}^\phi = \mathbf{x} + \mathbf{u}_0, \quad \text{on } \Gamma_0^\phi \subseteq \partial\Omega^\phi, \quad \mathbf{x} \in \partial\Omega, \quad (2c)$$

where  $\mathbf{f}^\phi : \Omega^\phi \rightarrow \mathbb{R}^3$  is a body force (density body force per unit volume in the deformed configuration),  $\mathbf{g}^\phi : \Gamma^\phi \rightarrow \mathbb{R}^3$  is a surface force, and  $\mathbf{u}_0$  is a given function describing the Dirichlet boundary conditions. The operator  $\operatorname{div}^\phi$  denotes the divergence operator taken with respect to  $\phi(\mathbf{x})$ . Also, we denote with

- $\mathbf{T}$  the *1st Piola–Kirchhoff stress*; a non-symmetric stress tensor  $\mathbf{T} : \bar{\Omega} \rightarrow \mathbb{M}^3$ , defined by the Piola transformation

$$\mathbf{T} = J\mathbf{T}^\phi \mathbf{F}^{-\top}, \quad (3)$$

- $\mathbf{S}$  the *2nd Piola–Kirchhoff stress*; a symmetric stress tensor  $\mathbf{S} : \bar{\Omega} \rightarrow \mathbb{S}^3$  defined by

$$\mathbf{S} = \mathbf{F}^{-1}\mathbf{T}. \quad (4)$$

For hyperelastic materials the 2nd Piola–Kirchhoff stress is linearly related to the elastic strain by *Hooke's law*

$$\mathbf{S}(\mathbf{u}) = \mathbf{C} : \mathbf{e}(\mathbf{u}), \quad (5)$$

where  $\mathbf{C} \in \mathbb{R}^{3 \times 3 \times 3 \times 3}$  denotes the fourth-order *elasticity tensor*. The components of the elasticity tensor are symmetric in the  $(i, j)$  and  $(k, l)$  index pair, hence it is equipped with the symmetry relations  $C_{ijkl} = C_{jikl} = C_{ijlk} = C_{klij}$ . The “:” operator stands for the tensor contraction and results in tensors of order reduced by two. In tensor notation, (5) can be expressed as

$$S_{ij} = C_{ijkl}e_{kl}, \quad (6)$$

by using the Einstein sum convection. Equivalently, due to the symmetry of the tensors involved, (6) can be compressed by using the *Voigt* contraction. Let

$$\mathbf{S} = \begin{pmatrix} S_{11} & S_{12} & S_{13} \\ \text{sym.} & S_{22} & S_{23} \\ & & S_{33} \end{pmatrix}, \quad \text{and} \quad \mathbf{e} = \begin{pmatrix} e_{11} & e_{12} & e_{13} \\ \text{sym.} & e_{22} & e_{23} \\ & & e_{33} \end{pmatrix}$$

be the stress and strain tensors, respectively. Then, the Voigt contraction yields a vector in  $\mathbb{R}^6$  and for the stress and strain it is defined by

$$\begin{aligned} \mathbf{S}^V &:= (S_{11}, S_{22}, S_{33}, S_{23}, S_{13}, S_{12})^\top \\ \mathbf{e}^{\bar{V}} &:= (e_{11}, e_{22}, e_{33}, 2e_{23}, 2e_{13}, 2e_{12})^\top. \end{aligned}$$

Note that the off-diagonal strain components are multiplied by two, so that

$$\mathbf{S}^V \mathbf{e}^{\bar{V}} = S_{ij}e_{ij} = \mathbf{S} : \mathbf{e} = 2F_e,$$

where  $F_e$  is the *free energy*. The above compression means that we do not have to distinguish between scalar multiplication of two Voigt contracted vectors in  $\mathbb{R}^6$  or tensor contraction between two tensors of second order. The Voigt notation can also be used to compress higher order tensors as well as products between tensors of different ranks. For the elasticity tensor  $\mathbf{C}$  the Voigt notation results in a  $\mathbb{R}^{6 \times 6}$  tensor, and will be discussed later in Section 3.3.

### 2.1.1 Elasticity problem in reference configuration

The system (2) in the deformed configuration involves the unknown deformation  $\mathbf{x}^\phi = \phi(\mathbf{x})$ . Moreover, unless we consider elastic deformations of solids under the assumption that the Eulerian domain is unchanged, in most problems the deformed domain  $\Omega^\phi$  is also unknown. Hence, we seek an invariant transformation into the reference configuration that retains the divergence structure and physical properties of the system [4]. Define  $\mathbf{f}(\mathbf{x}) := J \mathbf{f}^\phi(\mathbf{x}^\phi)$  to be the density of the applied body force per unit volume in the reference configuration. Similarly let  $\mathbf{g}(\mathbf{x}) := J \|\mathbf{F}^{-\top} \mathbf{n}\| \mathbf{g}^\phi(\mathbf{x}^\phi)$  be the density of the applied surface forces per unit area, where  $\mathbf{n} \in S_2$  is the normal vector to an area element  $d\mathbf{a}$ . An arbitrary volume  $V^\phi \subset \Omega^\phi$  in the deformed space is transformed to the reference configuration by the following relations:

$$\int_{V^\phi} d\mathbf{x}^\phi = \int_V J d\mathbf{x}, \quad \int_{\partial V^\phi} d\mathbf{a}^\phi = \int_{\partial V} J \|\mathbf{F}^{-\top} \mathbf{n}\| d\mathbf{a}, \quad \text{and} \quad \mathbf{n}^\phi := \frac{1}{\|\mathbf{F}^{-\top} \mathbf{n}\|} \mathbf{F}^{-\top} \mathbf{n}.$$

Then, by utilizing (3) and integrating (2a) and (2b) over the volume  $V^\phi$  and its boundary  $\partial V^\phi$ , respectively, we obtain the following Lagrangian system in the material configuration:

$$-\operatorname{div}(\mathbf{T}(\mathbf{x})) = \mathbf{f}(\mathbf{x}), \quad \forall \mathbf{x} \in \Omega, \quad (7a)$$

$$\mathbf{T}(\mathbf{x})\mathbf{n} = \mathbf{g}(\mathbf{x}), \quad \forall \mathbf{x} \in \Gamma \subseteq \partial\Omega \text{ and } \forall \mathbf{n} \in S_2, \quad (7b)$$

$$\mathbf{u}(\mathbf{x}) = \mathbf{u}_0, \quad \text{on } \Gamma_0 \subseteq \partial\Omega. \quad (7c)$$

Next, we will develop a version of (7) for a composite structure which experiences strain due to different lattice constants of the consisting materials.

## 2.2 Energy-based description of elasticity model for heterostructures

For hyperelastic materials, the solution of (7) for conservative applied forces is equivalent to finding the stationary point of the *total energy* [4] given by

$$E(\psi) = \int_{\bar{\Omega}} W(\mathbf{x}, \nabla \psi(\mathbf{x})) d\mathbf{x} - \left( \int_{\Omega} f(\mathbf{x}) \psi(\mathbf{x}) d\mathbf{x} + \int_{\Gamma} g(\mathbf{x}) \psi(\mathbf{x}) d\mathbf{a} \right),$$

for all admissible deformations  $\psi : \bar{\Omega} \rightarrow \mathbb{R}^3$ , such that  $\det(\psi) > 0$ , and  $\psi = \phi_0$  on  $\Gamma_0$ . The function  $W : \bar{\Omega} \times \mathbb{M}_+^3 \rightarrow \mathbb{R}$  is called the *stored energy function* and for hyperelastic materials it defines the 1st Piola–Kirchhoff stress by [4, Theorem 4.4-1]

$$\mathbf{T}(\mathbf{x}) = \frac{\partial W(\mathbf{x}, \mathbf{F})}{\partial \mathbf{F}}, \quad \text{for all } \mathbf{x} \in \bar{\Omega}, \mathbf{F} \in \mathbb{M}_+^3. \quad (8)$$

For homogeneous structures in equilibrium, the stored energy function depends on the choice of the strain tensor and the hyperelastic model in question. In this paper, we consider the St. Venant–Kirchhoff model [29, 30]; hence, in the present of the Green-Lagrange strain tensor (1) the stored energy function for *homogeneous* structures is given by

$$W(\mathbf{x}, \mathbf{F}) = \frac{1}{8} (\mathbf{F}^T \mathbf{F} - \mathbf{I}) : (\mathbf{C} : (\mathbf{F}^T \mathbf{F} - \mathbf{I})). \quad (9)$$

Differentiating (9) with respect to  $\mathbf{F}$  gives  $\mathbf{T} = \mathbf{F}(\mathbf{C} : \varepsilon)$  which is consistent with (4) and (5) in the case the total strain equals the elastic strain.

For composite structures is not straightforward to derive the stored energy at the reference configuration. This is because the structure is prestrained due to the induced strain at the connecting interface between the composite materials. At the interface the distance between atoms is different from the natural unstrained state when considering both materials separately. In order to describe the stored energy function in the reference configuration, we need a transformation that maps the prestrained state to a stress-free configuration.

Consider a multi-material domain  $\bar{\Omega} = \cup_{p=1}^P \bar{\Omega}_p \subset \mathbb{R}^3$  and assume that  $\bar{\Omega}_p$  are prestrained volumes (in the reference configuration) with different material structures, as shown in Figure 1 for the case of  $P = 2$ . We assume that an arbitrary (infinitesimally small) volume  $V \subset \bar{\Omega}_p$  relaxes to an unstrained (and energy minimizing) state by an affine deformation  $\psi(\mathbf{x}) := \mathbf{M}_p \mathbf{x} = \tilde{\mathbf{x}}$ , where  $\mathbf{M}_p \in \mathbb{M}^3$  is independent of  $V$  [2]. We define the stress-free state of domain  $\bar{\Omega}_p$  to be  $\tilde{\Omega}_p := \psi(\bar{\Omega}_p) = \mathbf{M}_p \bar{\Omega}_p$ . The *elastic (or strain) energy* of a deformation  $\tilde{\phi}$  related to  $\tilde{\Omega}_p$  is given by

$$\int_{\tilde{\Omega}_p} W(\tilde{\mathbf{x}}, \nabla_{\tilde{\mathbf{x}}} \tilde{\phi}(\tilde{\mathbf{x}})) d\tilde{\mathbf{x}}.$$

Following [2, 12], the original deformation  $\phi : \bar{\Omega}_p \rightarrow \mathbb{R}^3$  and  $\tilde{\phi}$  are related by  $\phi(\mathbf{x}) = \tilde{\phi}(\psi(\mathbf{x}))$ ,

and thus we can project the elastic energy on  $\tilde{\Omega}_p$  to the reference configuration  $\bar{\Omega}_p$  by [2]

$$\begin{aligned} \int_{\tilde{\Omega}_p} W(\tilde{\mathbf{x}}, \nabla_{\tilde{\mathbf{x}}} \tilde{\phi}(\tilde{\mathbf{x}})) d\tilde{\mathbf{x}} &= \int_{\psi(\bar{\Omega}_p)} W(\tilde{\mathbf{x}}, \nabla_{\tilde{\mathbf{x}}} \tilde{\phi}(\tilde{\mathbf{x}}) \mathbf{M}_p^{-1}) d\tilde{\mathbf{x}} \\ &= \int_{\psi(\bar{\Omega}_p)} W(\tilde{\mathbf{x}}, \nabla_{\mathbf{x}} \phi(\mathbf{x}) \mathbf{M}_p^{-1}) d\tilde{\mathbf{x}} \\ &= \int_{\bar{\Omega}_p} W(\mathbf{x}, \mathbf{F} \mathbf{M}_p^{-1}) \det(\mathbf{M}_p) d\mathbf{x}. \end{aligned}$$

For each  $\mathbf{x} \in \cup_p \bar{\Omega}_p$  the total deformation  $\mathbf{F}$  can be expressed as a multiplicative composition of the elastic deformation  $\mathbf{F}_{\text{el}}$  and predeformation  $\mathbf{M}$ , namely  $\mathbf{F} = \mathbf{F}_{\text{el}} \mathbf{M}$  [22]. In each region  $\bar{\Omega}_p$ , the predeformation  $\mathbf{M} = \mathbf{M}(\mathbf{x})$  is given by a constant matrix  $\mathbf{M}_p$ . Therefore, the stored energy function for the heterostructure in the reference configuration is defined by

$$\widehat{W}(\mathbf{x}, \mathbf{F}) := \det(\mathbf{M}(\mathbf{x})) W(\mathbf{x}, \mathbf{F} \mathbf{M}^{-1}(\mathbf{x})) = \det(\mathbf{M}(\mathbf{x})) W(\mathbf{x}, \mathbf{F}_{\text{el}}(\mathbf{x})). \quad (10)$$

We define the elastic Green-Lagrange strain of the heterostructure by

$$\mathbf{e} := \boldsymbol{\varepsilon}(\mathbf{F}_{\text{el}}) = \frac{1}{2}(\mathbf{F}_{\text{el}}^{\top} \mathbf{F}_{\text{el}} - \mathbf{I}). \quad (11)$$

Utilizing the equation  $\mathbf{F}_{\text{el}} = \mathbf{F} \mathbf{M}^{-1}$  along with (1), we can expand and rearrange terms in (11) to arrive at the following relation between the elastic and total strain:

$$\mathbf{e} = \mathbf{M}^{-\top} \boldsymbol{\varepsilon}(\mathbf{F}) \mathbf{M}^{-1} - \frac{1}{2}(\mathbf{I} - \mathbf{M}^{-\top} \mathbf{M}^{-1}).$$

The second term in the above equation characterises the pre-strain  $\boldsymbol{\varepsilon}_0 := \frac{1}{2}(\mathbf{I} - \mathbf{M}^{-\top} \mathbf{M}^{-1})$  and it is natural to assume that depends on the material's lattice constant. Hence, we consider the predeformation matrix with entries

$$M_{ij}(\mathbf{x}) = (1 + \nu_i(\mathbf{x})) \delta_{ij}, \quad i, j \in \{1, 2, 3\},$$

where  $\delta_{ij}$  is the Kronecker delta and

$$\nu_i(\mathbf{x}) := \frac{l_i(\mathbf{x}) - l_{i,\text{ref}}}{l_i(\mathbf{x})}, \quad i \in \{1, 2, 3\}, \quad (12)$$

is the relative component-wise difference of the lattice constant to some reference parameters  $l_{i,\text{ref}}$ ,  $i \in \{1, 2, 3\}$ . For each  $\mathbf{x} \in \bar{\Omega}_p$ , the vector  $\mathbf{l}(\mathbf{x}) = (a(\mathbf{x}), b(\mathbf{x}), c(\mathbf{x}))$  contains the lattice constants in each physical direction of the material in domain  $\bar{\Omega}_p$ . In general, the unit cell of a given crystal lattice may consist of sides with different lengths and angles. There are several reasonable options for the reference lattice constant  $\mathbf{l}_{\text{ref}}$ . For example,  $\mathbf{l}_{\text{ref}}$  could refer to the volumetric average of lattice constants in the composite structure; however, in most cases  $\mathbf{l}_{\text{ref}}$  is chosen to be the lattice constant of a bulk/core material [25].

In order to obtain the derivative of the stored energy function (10) it is convenient to use index notation. Using (9), we can rewrite (10) as

$$\widehat{W} = \frac{1}{2} \det(\mathbf{M}) C_{ijkl} e_{ij} e_{kl}. \quad (13)$$

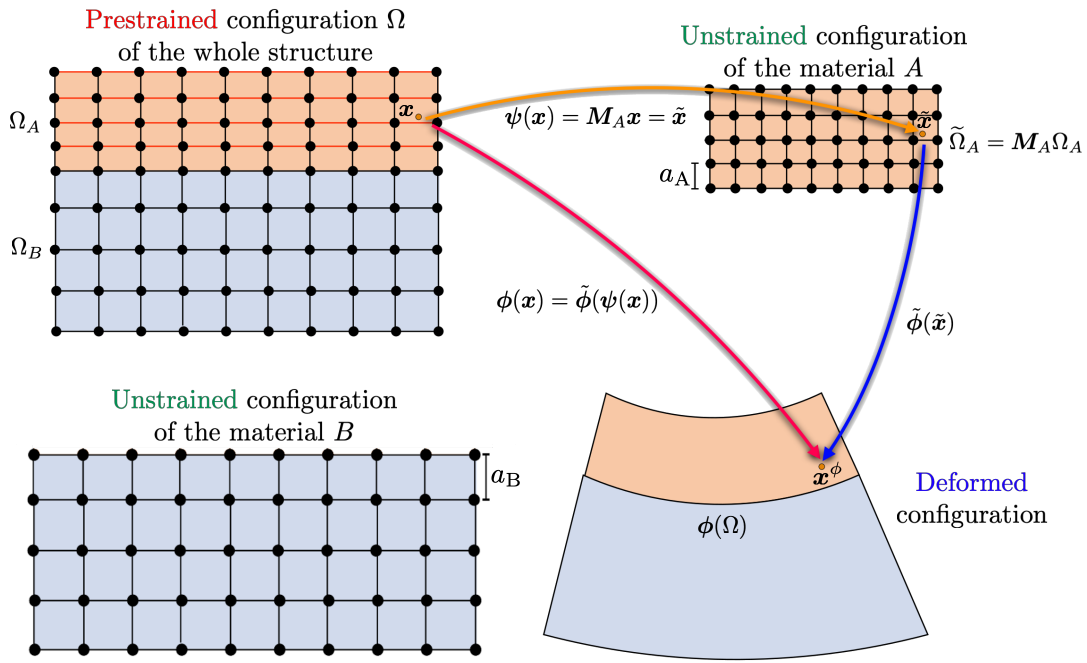


Figure 1: Prestrained (reference), unstrained and deformed configurations for a two-material structure.

It can be shown that the partial derivative of  $\widehat{W}$  with respect to an arbitrary element of  $\mathbf{F}$  yields  $\frac{\partial \widehat{W}}{\partial \mathbf{F}} = \det(\mathbf{M}) \mathbf{F} \mathbf{M}^{-1} (\mathbf{C} : \mathbf{e}) \mathbf{M}^{-\top}$  (see Appendix A). Using (8) and assuming no external forces, i.e.  $\mathbf{f} = \mathbf{0}$ , equation (7a) becomes

$$-\operatorname{div} (\det(\mathbf{M}(\mathbf{x})) \mathbf{F} \mathbf{M}^{-1}(\mathbf{x}) (\mathbf{C} : \mathbf{e}) \mathbf{M}^{-\top}(\mathbf{x})) = 0. \quad (14)$$

Equation (14) can be further simplified for the case of isotropic cubic crystal structures. In such case, the lattice constants are the same in each direction, i.e.,  $a(\mathbf{x}) = b(\mathbf{x}) = c(\mathbf{x})$ , for a given  $\mathbf{x} \in \overline{\Omega}_p$ . Therefore, (14) boils down to

$$-\operatorname{div} \left( \frac{1}{1 + \nu_1(\mathbf{x})} \mathbf{F} (\mathbf{C} : (\boldsymbol{\varepsilon} - \widehat{\boldsymbol{\varepsilon}}_0)) \right) = 0, \quad (15)$$

where  $\widehat{\boldsymbol{\varepsilon}}_0 = \nu_1(\mathbf{x}) \left( 1 + \frac{\nu_1(\mathbf{x})}{2} \right) \mathbf{I}$ , and  $\nu_1(\mathbf{x}) = \frac{a(\mathbf{x}) - l_{1,\text{ref}}}{a(\mathbf{x})} = \nu_2(\mathbf{x}) = \nu_3(\mathbf{x})$ .

### 3 Nanowire heterostructures and bimetallic beams

In this section, we introduce the hexagonal nanowire as our main application, as well as a bimetallic beam which serves as a simpler model for comparison purposes.

#### 3.1 Alloy nanowire

The primary focus of this study is on a nanowire heterostructure, which comprises two distinct regions: a core region and a stressor region. We use semiconductor materials. The core region

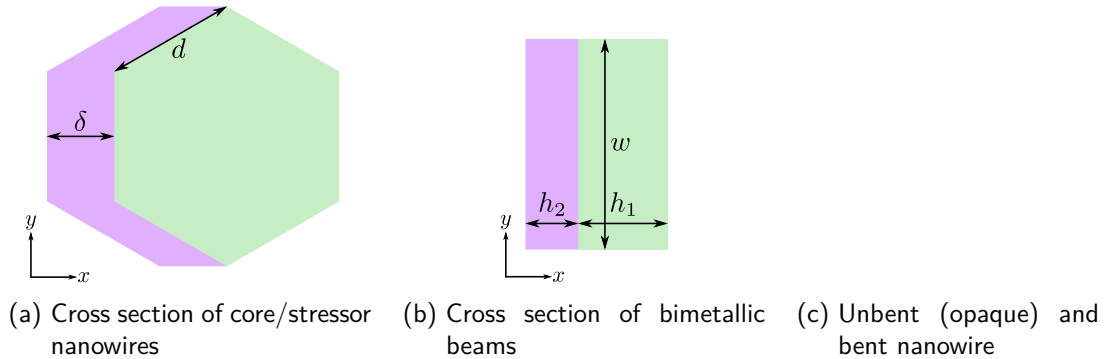


Figure 2: *Panels (a) & (b)*: Nanowire's and bimetallic beam's cross sections. The green region corresponds to the core material and the purple to the stressor. *Panel (c)*: Simulation results showing a 2000 nm long unbent and deformed GaAs/In<sub>0.5</sub>Al<sub>0.5</sub>As nanowire with  $d = 50/\sqrt{3}$  nm and  $\delta = 10$  nm.

is composed of GaAs and is characterized as a regular hexagon with side length  $d$ . On the other hand, the stressor region consists of an In <sub>$x$</sub> Al <sub>$1-x$</sub> As alloy, where  $x \in [0, 1]$ , with a thickness of  $\delta$ . Usually the hexagonal sides of the core region  $d$  is about 30 – 60 nm and the thickness  $\delta$  of the stressor is 5 – 25 nm. The stressor region covers half of the core region and its specific configuration was chosen due to its relevance and potential applications in nanowire devices and technologies. For the purposes of this work, we specifically focus on the cross-sectional shape depicted in Figure 2a. It is worth mentioning that other cross-sectional shapes, such as multilayer nanowires or cylindrical nanowires [3, 17], are also possible and could be considered in future investigations.

The heterostructure's lattice mismatch between the GaAs core and the In <sub>$x$</sub> Al <sub>$1-x$</sub> As stressor results in strain accumulation at the interface, leading to significant deformations, as illustrated in Figure 2c. Understanding and analyzing these large deformations are key objectives of this study.

### 3.2 Bimetallic beam

In addition to the nanowire heterostructures, we also explore the behavior of a bimetallic beam with a rectangular cross-section, as shown in Figure 2b. The inclusion of the bimetallic beam tests allows us to verify the accuracy of our model and assess the reliability of the numerical solution. Since there exists a considerable body of research on the bending behavior of bimetallic beams, we can compare our results with well-established findings to ensure the validity of our approach. The beam consists of two different materials, where the thickness of one material is usually greater than the other, i.e.,  $h_1 > h_2$ . Similar to the nanowires, the bending of the bimetallic beam is triggered by the lattice mismatch between the two constituent materials.

Physical quantity (units)	GaAs		$\text{In}_x\text{Al}_{1-x}\text{As}$	
	symbol	value	symbol	value
elastic component (GPa)	$C_{11}$	122.1	$C_{11}$	$83.29x + 125.0(1 - x)$
	$C_{12}$	56.6	$C_{12}$	$45.26x + 53.4(1 - x)$
	$C_{44}$	60.0	$C_{44}$	$39.59x + 54.2(1 - x)$
ZB-001 lattice constant (Å)	$a$	5.6532	$a$	$6.0583x + 5.6611(1 - x)$
	$b$	5.6532	$b$	$6.0583x + 5.6611(1 - x)$
	$c$	5.6532	$c$	$6.0583x + 5.6611(1 - x)$
ZB-111 lattice constant (Å)	$a$	$5.6532/\sqrt{2}$	$a$	$(6.0583x + 5.6611(1 - x))/\sqrt{2}$
	$b$	$5.6532/\sqrt{2}$	$b$	$(6.0583x + 5.6611(1 - x))/\sqrt{2}$
	$c$	$5.6532(2/\sqrt{3})$	$c$	$(6.0583x + 5.6611(1 - x))(2/\sqrt{3})$

Table 1: Material parameters of GaAs and  $\text{In}_x\text{Al}_{1-x}\text{As}$  for different crystal structures [31].

### 3.3 Crystal structures and material parameters

We consider two types of crystal structures: zincblende-001 (ZB-001) and zincblende-111 (ZB-111). Let  $\mathbf{C}^{001}$  and  $\mathbf{C}^{111}$  be the  $\mathbb{R}^{6 \times 6}$  Voigt representations of their respective elasticity tensors, given by

$$\mathbf{C}^{001} := \begin{pmatrix} C_{11} & C_{12} & C_{12} & 0 & 0 & 0 \\ C_{12} & C_{11} & C_{12} & 0 & 0 & 0 \\ C_{12} & C_{12} & C_{11} & 0 & 0 & 0 \\ 0 & 0 & 0 & C_{44} & 0 & 0 \\ 0 & 0 & 0 & 0 & C_{44} & 0 \\ 0 & 0 & 0 & 0 & 0 & C_{44} \end{pmatrix},$$

$$\mathbf{C}^{111} := \begin{pmatrix} C_{11}^{\text{ZB}} & C_{12}^{\text{ZB}} & C_{13}^{\text{ZB}} & 0 & C_{15}^{\text{ZB}} & 0 \\ C_{12}^{\text{ZB}} & C_{11}^{\text{ZB}} & C_{13}^{\text{ZB}} & 0 & -C_{15}^{\text{ZB}} & 0 \\ C_{13}^{\text{ZB}} & C_{13}^{\text{ZB}} & C_{33}^{\text{ZB}} & 0 & 0 & 0 \\ 0 & 0 & 0 & C_{44}^{\text{ZB}} & 0 & -C_{15}^{\text{ZB}} \\ C_{15}^{\text{ZB}} & -C_{15}^{\text{ZB}} & 0 & 0 & C_{44}^{\text{ZB}} & 0 \\ 0 & 0 & 0 & -C_{15}^{\text{ZB}} & 0 & C_{66}^{\text{ZB}} \end{pmatrix}.$$

The ZB-001 crystals exhibit cubic symmetry, and the surface of the unit cell has a square shape when cut perpendicular to the [001] direction. The Miller index system is used for crystallographic directions [19, 20]. When it comes to anisotropic materials, the simplest case contains three independent elements. On the other hand, isotropic ZB-001 materials have only two independent elements expressed in terms of the Lamé parameters, namely  $C_{11} = \lambda + 2\mu$ ,  $C_{12} = \lambda$ , and  $C_{44} = 2\mu$ . The ZB-111 anisotropic crystals have a hexagonal symmetry and their atomic layers are stacked along the [111] direction. The corresponding elasticity tensor  $\mathbf{C}^{111}$  can be obtained by properly rotating the  $\mathbf{C}^{001}$  tensor, and consequently, its elements can be expressed linearly in terms of  $C_{11}$ ,  $C_{12}$ , and  $C_{44}$  [25]. Table 1 displays the elasticity parameters and lattice constants used in the simulations. All material values are taken from [31].

### 3.4 Boundary conditions

At equilibrium, we assume that no body or surface forces are applied, i.e.,  $\mathbf{f}(\mathbf{x}) = \mathbf{0}$  for all  $\mathbf{x} \in \bar{\Omega}$ , and  $\mathbf{g}(\mathbf{x}) = \mathbf{0}$  for all  $\mathbf{x} \in \Gamma \subseteq \partial\Omega$ . We solve the momentum equation (14) for the displacement  $\mathbf{u} = \mathbf{u}(\mathbf{x}) \in \mathbb{R}^3$ ,  $\mathbf{x} \in \mathbb{R}^3$ , with homogeneous Neumann boundary conditions

$$\mathbf{T}(\mathbf{x})\mathbf{n} = \mathbf{0}$$

at all facets except one where we apply Dirichlet boundary conditions  $\mathbf{u} = \mathbf{0}$ . Then, we can calculate the overall deformation  $\phi(\mathbf{x}) = \mathbf{x} + \mathbf{u}(\mathbf{x})$ , and hence the total and elastic strain via (1) and (11).

## 4 Theoretical derivation of curvature

The classical bending theory, formally proposed by Timoshenko [27], was originally designed to explain the behavior of bimetallic thermostats subjected to uniform heating. However, when dealing with nanoscale heterostructures, where the bending is not caused by a temperature change, the behavior can deviate significantly from that of macroscopic counterparts. For instance, the bending of an ultrathin Ge/Si film grown on a thin SiO<sub>2</sub> substrate [15, 10]. Other factors such as piezoelectric [16], flexoelectric [34, 32], and quantum effects [9] may also affect the bending.

Nevertheless, if we focus solely on mechanical bending and disregard atomic-level details of the film structure, polarization, and quantum effects, the continuum theory can still provide an adequate description of the mechanical bending in nanostructures. Various studies have examined the bending of strained nanoscale bimetallic strips, even when the films are only a few nanometers thick. For example, derivations of the diameter of (In,Ga)As/GaAs and Si nanotubes formed by rolled-up films have been compared to experiments in [5] and [26], respectively. Moreover, these analyses have been extended to incorporate surface stress effects [33].

In the following, we extend the bending theory to encompass nanoscale structures with arbitrary cross sections by combining concepts from the work of Zang and Liu [33] and Lewis et al. [14]. Specifically, we derive analytic expressions for the curvature and interface lattice constant of bent asymmetric heterostructured nanowires, by minimizing the strain energy along the bending axis. As a consequence, we can characterize the profile of the axial elastic strain on a cross section. We demonstrate that, under a prestrain assumption, the energy-based approach is equivalent to Timoshenko's mechanical derivation, which involves balancing forces in the axial direction.

### 4.1 Energy-based approach

Assume that the heterostructure is coherent throughout the whole domain and consider an arbitrary cross section of the material. Also, we consider the bending direction to be perpendicular to the selected cross section. For elastic materials satisfying (5), the simplest strain energy model takes into account a linear relation between stress and strain along the bending axis. In the following we consider the projection of strain and stress onto the  $x - y$  plane for a given  $z^*$  in the reference configuration. It is sufficient to consider the axial elastic strain

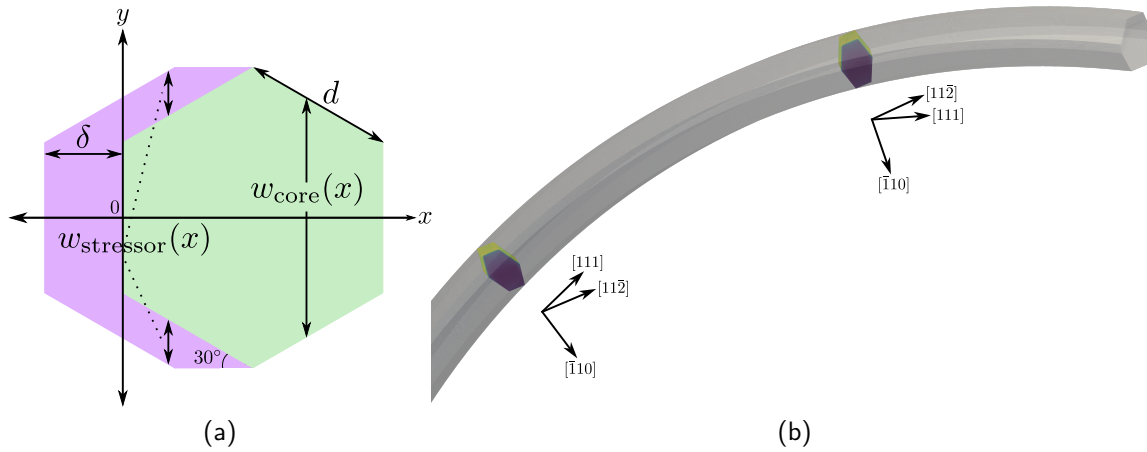


Figure 3: *Left*: Graphical projection of a nanowire's cross section in the  $x - y$  plane of the reference configuration. The left polygon region corresponds to stressor domain  $\bar{\Omega}_{\text{stressor}}$  and the hexagon to the core material domain  $\bar{\Omega}_{\text{core}}$ . The functions  $w_{\text{core}}(x)$  and  $w_{\text{stressor}}(x)$  represent the width of the core and stressor regions, respectively, as they vary with the distance  $x$  from the origin. For simplicity, the coordinate system is conveniently centered at the middle of the vertical interface that separates the two materials. The parameter  $d$  corresponds to length of each side of the hexagonal core and  $\delta$  to the thickness of the stressor on the left side of the wire. *Right*: Positions of deformed cross sections for a ZB-111 nanowire. At each cross section, the spatial coordinate axes  $(X, Y, Z)$  are aligned along the  $([\bar{1}10], [11\bar{2}], [111])$  crystallographic directions.

$e_{33}(x, y, z^*)$  and the corresponding axial stress  $\sigma_{33}(x, y, z^*)$  of the cross section [14]. Suppose that the material bends along the  $x$ -axis, then the *strain energy* per unit length is given by

$$\mathcal{E} := \frac{1}{2} \int Y(x)w(x)\epsilon^2(x)dx, \quad (16)$$

where  $\epsilon(x) = e_{33}(x, 0, z^*)$  is the axial component of the elastic strain along the middle line,  $Y(x) = \sigma_{33}(x, 0, z^*)/\epsilon(x)$  is the longitudinal Young's module, and  $w(x)$  is the width of material at position  $x$  (e.g., see Figure 3a). The function  $w(x)$  depends on the choice of the cross section and has to be defined in each material region. In a deformed configuration the strain energy is minimal; therefore, by expressing  $\epsilon(x)$  in terms of the curvature and minimizing the total strain energy of the system yields an expression for the curvature of the bent heterostructure.

#### 4.1.1 Application to core/stressor nanowires

We establish a moving spatial coordinate system in the deformed space related to the crystallographic directions of the nanowire. The bending direction is represented by the  $Z$ -axis, while the cross-sectional plane lies in the  $X - Y$  plane, as illustrated in Figure 3b. The orientation of the coordinate axes is influenced by the crystal structure of the nanowire. Consequently, for the two crystal structures discussed in Section 3.3, the  $(X, Y, Z)$  axes are defined using the Miller indexing. Therefore, the coordinate axes are aligned along the  $([100], [010], [001])$ , and  $([\bar{1}10], [11\bar{2}], [111])$  directions for ZB-001, and ZB-111 crystals, respectively [25, 23].

Mathematically speaking we choose the cross section in the reference configuration such that in the deformed space it is normal to the  $Z$ -axis (see Figure 3b). For composite structures, the

axial strain on such cross section depends linearly on the distance from the fixed origin with the slope determined by the curvature [14]. In the case of a bent core/stressor nanowire with the stressor applied on the left side of the hexagon, as depicted in Figure 3, the axial elastic strain in the core region is given by

$$\epsilon_{\text{core}}(x) := \frac{l_{\text{inter}} - l_{\text{core}}}{l_{\text{core}}} - \kappa x, \quad 0 \leq x \leq \sqrt{3}d, \quad (17)$$

where  $\kappa$  is the curvature, and the lattice constant at the interface is denoted by  $l_{\text{inter}}$ . The axial elastic strain in the stressor region takes the form

$$\epsilon_{\text{stressor}}(x) := \epsilon_{\text{core}}(x) - \nu_{\text{m}}, \quad -\delta \leq x \leq \frac{\sqrt{3}}{2}d, \quad (18)$$

where  $\nu_{\text{m}}$  is the misfit strain  $\frac{l_{\text{stressor}} - l_{\text{core}}}{l_{\text{stressor}}}$  [33]. It is worth noting that in such case the axial strain is independent of the  $y$ -direction. Now, the function  $w(x)$  in (16) expresses the total material width at a given location  $x$ . Let the side of the core hexagon region be  $d$  and the width of the stressor be  $\delta$ , as shown in Figure 3a. We define  $w(x)$  separately in each region, thus, at the core it is given by

$$w_{\text{core}}(x) = \begin{cases} \frac{2}{\sqrt{3}}x + d, & 0 \leq x < \frac{\sqrt{3}}{2}d, \\ -\frac{2}{\sqrt{3}}x + 3d, & \frac{\sqrt{3}}{2}d \leq x \leq \sqrt{3}d, \\ 0, & \text{elsewhere.} \end{cases}$$

If  $\delta \leq \sqrt{3}d/2$ , then the width  $w(x)$  in the stressor region is

$$w_{\text{stressor}}(x) = \begin{cases} \frac{2}{\sqrt{3}}(\delta + x) + d, & -\delta \leq x \leq 0, \\ \frac{2}{\sqrt{3}}\delta, & 0 < x < \frac{\sqrt{3}}{2}d - \delta, \\ -\frac{2}{\sqrt{3}}x + d, & \frac{\sqrt{3}}{2}d - \delta \leq x \leq \frac{\sqrt{3}}{2}d, \\ 0, & \text{elsewhere.} \end{cases}$$

Similar expression for  $w_{\text{stressor}}(x)$  can be obtained for  $\delta > \sqrt{3}d/2$ . Finally, the Young's modulus can be calculated directly for each region based on the elasticity coefficients of the respective materials. Let  $\mathbf{C}^{\text{V}}$  be the Voigt notation of the elastic stiffness tensor  $\mathbf{C}$ . The inverse of  $\mathbf{C}^{\text{V}}$  is called the compliance matrix and can be expressed in an *engineering* form using *elastic engineering modules* as proposed by Lekhnitskii [13] and Ganczarski et al. [8]. In the case of a triclinic anisotropic material, equating the compliance matrix expressed in terms of the elasticity coefficients  $C_{ij}$  to its engineering counterpart provides relations for various material properties, including axial and shear moduli, Poisson ratios, Chencov's modules, and Rabinovich's modules (see [8, Chapter 1.4]). To determine the longitudinal axial Young's modulus, denoted as  $Y$ , one can use the reciprocal of the  $(\mathbf{C}^{\text{V}})_{33}^{-1}$  component. For a trigonal anisotropic material (ZB-111) the expression for the Young's modulus is

$$Y = C_{33}^{\text{ZB}} - \frac{2(C_{13}^{\text{ZB}})^2}{C_{11}^{\text{ZB}} + C_{12}^{\text{ZB}}}, \quad (19)$$

and for isotropic (ZB-100) materials is given by

$$Y = C_{11} - \frac{2C_{12}^2}{C_{11} + C_{12}}. \quad (20)$$

Clearly,  $Y_{\text{core}}$  and  $Y_{\text{stressor}}$  correspond to the Young's modulus in the core and stressor region, respectively, where the corresponding entries for the elasticity tensor are taken from Table 1.

Putting all together, the strain energy (16) for the case of core/stressor nanowires takes the form

$$\mathcal{E}(x; \kappa, l_{\text{inter}}) = \frac{1}{2} \int_{x \in \bar{\Omega}_{\text{core}}} Y_{\text{core}} w_{\text{core}}(x) \epsilon_{\text{core}}^2(x) dx + \frac{1}{2} \int_{x \in \bar{\Omega}_{\text{stressor}}} Y_{\text{stressor}} w_{\text{stressor}}(x) \epsilon_{\text{stressor}}^2(x) dx.$$

The deformed configuration of the system corresponds to the state of minimum energy. By minimizing the strain energy with respect to the curvature  $\kappa$  and the interfacial lattice constant  $l_{\text{inter}}$ , we can derive the following analytical expression for the equilibrium curvature:

$$\kappa = \frac{108d\delta (4\delta + 3\sqrt{3}d) Y_{\text{core}} Y_{\text{stressor}} \nu_m}{135\sqrt{3}d^4 Y_{\text{core}}^2 + 36d\delta (17d^2 + 8\delta^2 + 9\sqrt{3}d\delta) Y_{\text{core}} Y_{\text{stressor}} + 2\sqrt{3}\delta^2 (15d^2 + 16\delta^2) Y_{\text{stressor}}^2}. \quad (21)$$

Regarding the interface lattice constant, while it can also be obtained by minimizing the energy, it involves a much more complex function. Therefore, for the sake of simplicity, we omit its detailed expression here. The lengthy derivation is given in the supplementary material <sup>1</sup>.

By presenting analytical expressions for the curvature and interface lattice constant, we can fully describe the axial elastic strain. For a bending direction along the  $z$ -axis, the axial component of the elastic strain on a given cross section located at  $z = z^*$  can be determined from equations (17) and (18), yielding

$$e_{33}(x, y, z^*) = \begin{cases} \epsilon_{\text{core}}(x), & (x, y) \in \bar{\Omega}_{\text{core}}, \\ \epsilon_{\text{stressor}}(x), & (x, y) \in \bar{\Omega}_{\text{stressor}}. \end{cases} \quad (22)$$

Later in Section 5.2 we compare (22) with its numerical counterpart.

## 4.2 Equivalence to Timoshenko's formula

Notice that in our model the stored energy function  $W$  in (8) depends only on the deformation gradient  $\mathbf{F}$ , and consequently on the strain. Since no other physical quantities, for instance electric field, influence the deformation exerted on the heterostructure, then the curvature of the bending can be described in a purely mechanical fashion. The length of the nanowires is on the order of micrometers and each composite material is a few nanometers thick. Therefore, at such scales the dynamics of the system can be adequately described by classical mechanics without relying on quantum effects that play a crucial role at subatomic scales. Furthermore, we assume that the material in each region is homogeneous through the structure's length, and cross-sections originally perpendicular to the bending axis become perpendicular to the curved axis of the structure.

With these considerations we can obtain analytic expressions for the curvature based on the bending analysis of a bimetallic beam due to uniform heating. This approach was introduced by Timoshenko [27] and is an extension of the Euler-Bernoulli beam bending theory. It takes into account the bending moment couple at equilibrium applied at the bearing surface axis, and the elongation occurring in the longitudinal fibres of each material due to thermal expansion and

<sup>1</sup><https://doi.org/10.5281/zenodo.10223704>

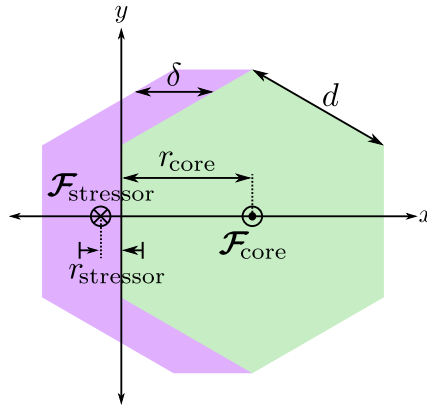


Figure 4: Schematic of the acting forces on the nanowire's cross section. The outwards force  $\mathcal{F}_{\text{core}}$  acts on the center of the hexagonal core region expanding the core material. The inwards force  $\mathcal{F}_{\text{stressor}}$  compresses the stressor and is applied at the centroid of the stressor region. The forces are at distances  $r_{\text{core}}$  and  $r_{\text{stressor}}$ , respectively, from the vertical interface separating the two regions (reference axis). At the deformed configuration the nanowire is at equilibrium and  $\mathcal{F}_{\text{core}} = -\mathcal{F}_{\text{stressor}}$ .

shear effects. In our derivation we replace the term that corresponds to the thermal expansion with a term that describes the fractional change in length due to lattice constant mismatch.

In the rest of this subsection we review the main concepts of the analysis applied to a two-material compound nanostructure. At the end, we demonstrate under which conditions Timoshenko's formula for the curvature is equivalent to the energy-based derivation of Section 4.1.

Consider a nanowire that combines two materials attached to each other with cross section as shown in Figure 2a. The materials in the core and stressor regions, depicted with green and purple colors respectively, have different axial lattice constants  $l_{\text{core}} < l_{\text{stressor}}$ . Since there are no external forces, at a given cross section perpendicular to the curved axis all forces acting over each region can be characterized by normal tensile and compressive forces.

We are interested in the bending moments generated by these forces with respect to the vertical interface separating the two materials, as depicted in Figure 4. Let  $\mathcal{F}_{\text{core}}$  be the axial tensile force vector acting outwards, expanding the core material, and let  $\mathcal{F}_{\text{stressor}}$  be the inwards axial compressive force compressing the stressor material with the largest lattice constant. Each force generates a bending moment  $\mathcal{M}_i = \mathbf{r}_i \times \mathcal{F}_i$ ,  $i \in \{\text{core}, \text{stressor}\}$ , with respect to the bearing axis, where  $\mathbf{r}_i$  is the position vector from the centroid of each region to the origin of the reference axis. Moreover, the magnitude of the bending moment is defined as the flexural rigidity of a given material divided by the radius of curvature. The flexural rigidity is given by the product of Young's module  $Y$  and the moment of inertia  $I$ . Therefore,  $\mathcal{M}_i = \kappa Y_i I_i$ ,  $i \in \{\text{core}, \text{stressor}\}$ , where  $\kappa$  is the bending curvature.

At equilibrium  $\mathcal{F}_{\text{core}} + \mathcal{F}_{\text{stressor}} = \mathbf{0}$ ; hence, both  $\mathcal{F}_{\text{core}}$  and  $\mathcal{F}_{\text{stressor}}$  must have the same magnitude  $\mathcal{F} = \mathcal{F}_{\text{core}} = \mathcal{F}_{\text{stressor}}$ . Let  $r = r_{\text{core}} + r_{\text{stressor}}$ . Then the force couple induces a torque moment  $\tau = \mathcal{F} r$  that equals the summation of all bending moments; hence,  $\mathcal{F} = (\mathcal{M}_1 + \mathcal{M}_2)/r$ .

Now, at the deformed configuration the length of the contact surface of the two materials can be estimated by considering the strain exerted at each material. Viewing the length from the

core's region perspective yields

$$L_{\text{core}} = L_0 \left( 1 + \nu_{\text{core}} + \frac{\mathcal{F}}{A_{\text{core}} Y_{\text{core}}} + \kappa r_{\text{core}} \right),$$

where  $L_0$  is the initial length of the nanowire in the reference configuration. The second term in the above expression describes the expansion produced by the relative difference of the material's lattice constant compared to a reference lattice constant. From (12) we have that  $\nu_{\text{core}} = (l_{\text{core}} - l_{\text{ref}})/l_{\text{core}}$ . The third term is the strain induced by the stress  $\mathcal{F}_{\text{core}}/A_{\text{core}}$  due to the force  $\mathcal{F}_{\text{core}}$  acting over the core area  $A_{\text{core}}$  (positive because the tensile force points out of the cross section). The last term is the additional length of the contact surface relative to line passing through the center of the core region (positive because the contact interface is the outer convex surface). Similarly the contact length in regards to stressor region is given by

$$L_{\text{stressor}} = L_0 \left( 1 + \nu_{\text{stressor}} - \frac{\mathcal{F}}{A_{\text{stressor}} Y_{\text{stressor}}} - \kappa r_{\text{stressor}} \right).$$

The minus sign is due to the fact that the force is compressive and the contact is on the inner surface. Since the two materials are connected, we have  $L_{\text{core}} = L_{\text{stressor}}$  where the two materials meet, and hence we can solve for the curvature.

For the cross section of Figure 4 we have that

$$\begin{aligned} r_{\text{core}} &= \frac{\sqrt{3}d}{2}, & I_{\text{core}} &= \frac{5\sqrt{3}d^4}{16}, & A_{\text{core}} &= \frac{3\sqrt{3}d^2}{2}, \\ r_{\text{stressor}} &= \frac{1}{8} (4\delta - \sqrt{3}d), & I_{\text{stressor}} &= \frac{5\delta d^3}{32} + \frac{\delta^3 d}{6}, & A_{\text{stressor}} &= 2d\delta. \end{aligned}$$

Details about the above derivations can be found in the supplementary material<sup>2</sup>. Substituting the above into  $L_{\text{core}} = L_{\text{stressor}}$  and solving for the curvature yields

$$\kappa = \frac{108d\delta (4\delta + 3\sqrt{3}d) Y_{\text{core}} Y_{\text{stressor}} (\nu_{\text{stressor}} - \nu_{\text{core}})}{135\sqrt{3}d^4 Y_{\text{core}}^2 + 36d\delta (17d^2 + 8\delta^2 + 9\sqrt{3}d\delta) Y_{\text{core}} Y_{\text{stressor}} + 2\sqrt{3}\delta^2 (15d^2 + 16\delta^2) Y_{\text{stressor}}^2}. \quad (23)$$

Assume now that all prestrain in the reference configuration lies in the stressor region. In such case  $l_{\text{ref}} = l_{\text{core}}$ ; therefore,  $\nu_{\text{core}} = 0$  and  $\nu_{\text{stressor}} = (l_{\text{stressor}} - l_{\text{core}})/l_{\text{stressor}} = \nu_{\text{m}}$ . Hence, (23) is equivalent to the curvature equation (21) derived in Section 4.1.1.

### 4.3 Bimetallic beam

Consider a bimetallic beam consisting of two materials with heights  $h_1$  and  $h_2$  as shown in Figure 2b. The core and shell sections are rectangles with areas  $A_i = wh_i$ ,  $i \in \{1, 2\}$ , where  $w(x) = w$  is the width of the bimetallic beam. In addition, let  $Y_1, Y_2$  be the Young's moduli and  $l_1, l_2$  the lattice constants of the core and shell region, respectively. Using (16) the strain energy for a bent bimetallic beam is

$$\mathcal{E}(x; \kappa, l_{\text{inter}}) = \frac{1}{2} \left( \int_{-h_1}^0 w Y_1 \epsilon_1^2(x) dx + \int_0^{h_2} w Y_2 \epsilon_2^2(x) dx \right).$$

<sup>2</sup><https://doi.org/10.5281/zenodo.10223704>

Assuming that  $l_2 \geq l_1$ , then the minimum strain energy at equilibrium occurs when the curvature is given by

$$\kappa = \frac{6(l_2 - l_1)h_1h_2Y_1Y_2(h_1l_1 + h_2l_2)}{h_2l_1^2Y_2(4h_1^3Y_1 + h_2^3Y_2) + 6h_1^2h_2^2l_1l_2Y_1Y_2 + h_1l_2^2Y_1(h_1^3Y_1 + 4h_2^3Y_2)}, \quad (24)$$

and reference lattice constant takes the form

$$l_{\text{inter}} = \frac{l_1l_2(h_2l_1Y_2(4h_1^3Y_1 + 3h_2h_1^2Y_1 + h_2^3Y_2) + h_1l_2Y_1(h_1^3Y_1 + 3h_2^2h_1Y_2 + 4h_2^3Y_2))}{h_2l_1^2Y_2(4h_1^3Y_1 + h_2^3Y_2) + 6h_1^2h_2^2l_1l_2Y_1Y_2 + h_1l_2^2Y_1(h_1^3Y_1 + 4h_2^3Y_2)}.$$

Equation (24) can be equivalently obtained by using the method of Section 4.2 and agrees with formulas given in [33]. Depending on the constitutive materials of the bimetallic beam, the Young's moduli can be expressed in terms of the coefficients of the corresponding elasticity tensor by using (19) or (20). Moreover, the expressions for the curvature and reference lattice constant can be simplified by writing them as functions of the lattice mismatch  $l_m = 100(l_2/l_1 - 1)$ , instead of the core's and shell's lattice constants.

## 5 Computational results

In this section we compare the analytical formulae (21) and (23) with the computed curvature from 3D simulations, thus allowing to validating our 3D implementation.

We test the performance of the elasticity formulation by solving the equation (15) by using finite element methods (FEM). We provide three examples to illustrate the effectiveness of the model and the numerical implementation. The first example demonstrates the bending increase of a bimetallic beam due to the growing lattice mismatch between its constituent materials. In the second example, we examine the strain profile of a bent GaAs/In<sub>0.25</sub>Al<sub>0.75</sub>As core/stressor nanowire. Finally, we compare the analytical derivations of curvature with numerical computations obtained from our simulations for both the bimetallic beam and nanowires in the last section.

Our implementation of the model in the programming language Julia can be found in the package `StrainedBandstructures.jl` and is based on the open-source finite element method package `GradientRobustMultiPhysics.jl` [18]. The weak formulation along with the details on how to solve the nonlinear system via Newton's method is provided in Appendix B. Along with this, exemplary meshes for the bimetallic beam and nanowire are also showcased there.

### 5.1 Deforming a bimetallic beam to a ring

This section showcases the model's capability to handle finite deformations through its numerical implementation. To illustrate this, we employ an initially straight bimetallic beam with a rectangular cross-section. The beam is fixed at one end. As we increase the lattice mismatch between the two constituent materials, both ends meet to form a ring.

In the reference configuration, the beam has a length of 2000 nm with a cross-section width  $w = 100$  nm and heights  $h_1 = 37.5$  nm and  $h_2 = 12.5$  nm, as shown in Figure 2b. The beam is discretised into 96,000 finite elements, with additional cells allocated at the interface

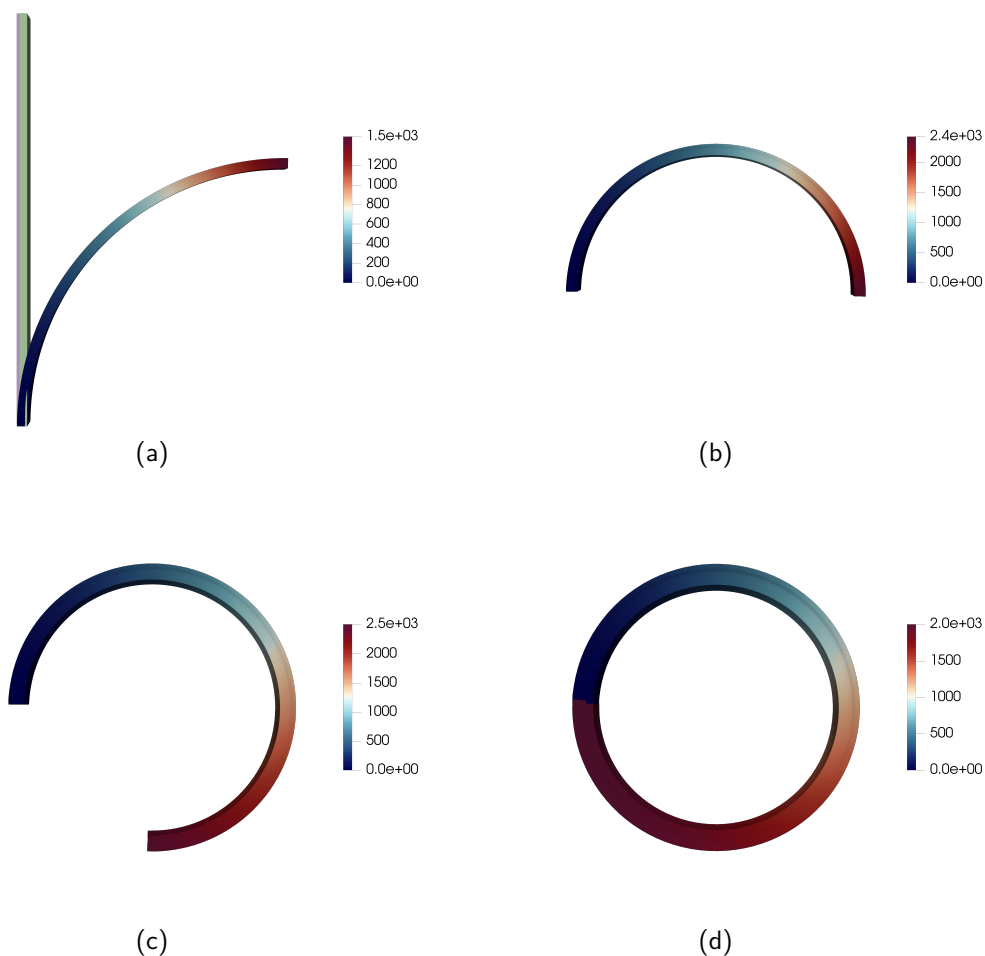


Figure 5: Sequence of bimetallic beams bending from a straight beam to a ring. Figure 5a also shows the bimetallic beam in its straight shape in the reference configuration. Initially the beam is 2000 nm long, and each material region has thickness  $w = 100$  nm and heights  $h_1 = 37.5$  nm and  $h_2 = 12.5$  nm. The bimetallic beam bends into 1/4, 1/2, 3/4, and full rings due to lattice mismatches  $l_m$  of 3.67%, 7.61%, 11.87%, and 16.48%, respectively. The legend displays the magnitude of the displacement  $\mathbf{u}$ .

where the two materials meet (see Figure 9b for a cross-section mesh). In this example, we assume isotropic materials with GaAs as the core material and  $\text{In}_{0.25}\text{Al}_{0.75}\text{As}$  as the shell, which behaves like a stressor. The Young moduli are  $Y_1 = 86.54$  GPa and  $Y_2 = 82.77$  GPa. However, instead of using the material's prescribed lattice constants, we use different ones. Specifically, for the core material ( $\mathbf{x} \in \Omega_1$ ), the lattice constant is denoted as  $a(\mathbf{x}) = l_0$ , while for the shell region ( $\mathbf{x} \in \Omega_2$ ), the lattice constant is given by  $a(\mathbf{x}) = l_0(1 + l_m)$ , where  $l_m$  represents the percentage increase of the shell lattice constant compared to that of the core. Figure 5 presents the displacement magnitude at different levels of lattice mismatch as the beam gradually forms a ring. Notice that the maximum displacement magnitude in Figures 5b-5d remains fairly consistent; however, the nature of deformations differs significantly. For a given bending angle, we can determine the relevant lattice mismatch to achieve the desired deformation. By expressing (24) in terms of the lattice mismatch, we can solve  $\theta/\kappa = L_0$  for  $l_m$ , where  $\theta$  is the bending angle and  $L_0$  the initial length of the beam.

While this example focuses on isotropic materials, similar deformations can be observed with

anisotropic materials. Thus, this ring simulation underscores the advantages of using a Lagrangian configuration. By formulating the constitutive model in the reference configuration, the fields naturally account for the underlying isotropic or anisotropic characteristics. This approach completely obviates the need for transforming material properties as the body undergoes large deformations. In the case of the ring example, setting all material parameters in the reference configuration is sufficient. As the beam transforms into a ring, the displacement and subsequent strain field ultimately conform to the physically correct configuration in the deformed space.

## 5.2 Strain profile for a GaAs/(In,Al)As nanowire

Nanowires are characterized by their high aspect ratio, with their length significantly exceeding their cross-sectional dimensions. Due to this high aspect ratio, the strain is uniformly distributed along the nanowire's length. Therefore, analyzing the strain profile solely at the cross-section of the nanowire adequately represents the overall strain distribution. The specific location of the cross-section within the nanowire becomes less significant as long as it is sufficiently far from the Dirichlet boundaries, where the boundary condition 7c has a noticeable effect.

In this section, we study the strain distribution in a ZB-(111) GaAs/In<sub>0.75</sub>Al<sub>0.25</sub>As core/stressor nanowire. In the reference configuration the nanowire has a length of 2000 nm and its cross section is depicted in Figure 2a, where  $d = 50/\sqrt{3}$  nm, and  $\delta = 10$  nm. The material parameters can be found in Table 1. First, we compare the axial elastic strain component  $e_{33}$  calculated by equation (22) and computed by our simulations. Figure 6 shows a very good agreement between (22) and numerical values. The analytic axial strain lies within the interval  $[-0.045277, 0.023470]$ , whereas the minimum and maximum computations are  $-0.042607$  and  $0.023667$ , respectively. The small discrepancy between the minimum values is due to the fact that (22) can be only derived in the reference configuration whereas the simulations show the elastic strain in the deformed space. The cross section is deformed the most near the bottom and top corners of the core region where the axial elastic strain takes its minimum values.

The strain distribution within nanowire structures is of paramount importance as it plays a pivotal role in determining the electrical and optoelectronic properties of such nanostructures [7]. The strain profile is visualized through a mid-length cross-section of the nanowire as shown in Figure 7. We focus on two primary aspects of the strain tensor: off-diagonal and diagonal components. Off-diagonal components provide crucial insights into the anisotropic nature of the (shear) strain field within the nanowire. These off-diagonal components represent the strain in the plane perpendicular to the nanowire axis and are indicative of the structural deformation caused by the core and stressor materials. In the left panel of the figure, we depict two off-diagonal elastic strain components ( $e_{13}$  and  $e_{23}$ ). The right panel of the figure, on the other hand, displays the diagonal as well as the off-diagonal  $e_{12}$  entries. The diagonal components reflect the strain along the principal axes of the nanowire and offer significant information about the axial strain. Meanwhile, the  $e_{12}$  component represents the shear strain in the  $x - y$  plane.

A notable observation from our analysis is that the diagonal and  $e_{12}$  components exhibit absolute magnitudes approximately four times larger than those of the off-diagonal components. This discrepancy in magnitude implies that the axial and shear strain in the  $x - y$  plane have a more substantial impact on the nanowire's overall behavior compared to the other off-diagonal components. Consequently, these dominant strain components are likely to exert a profound

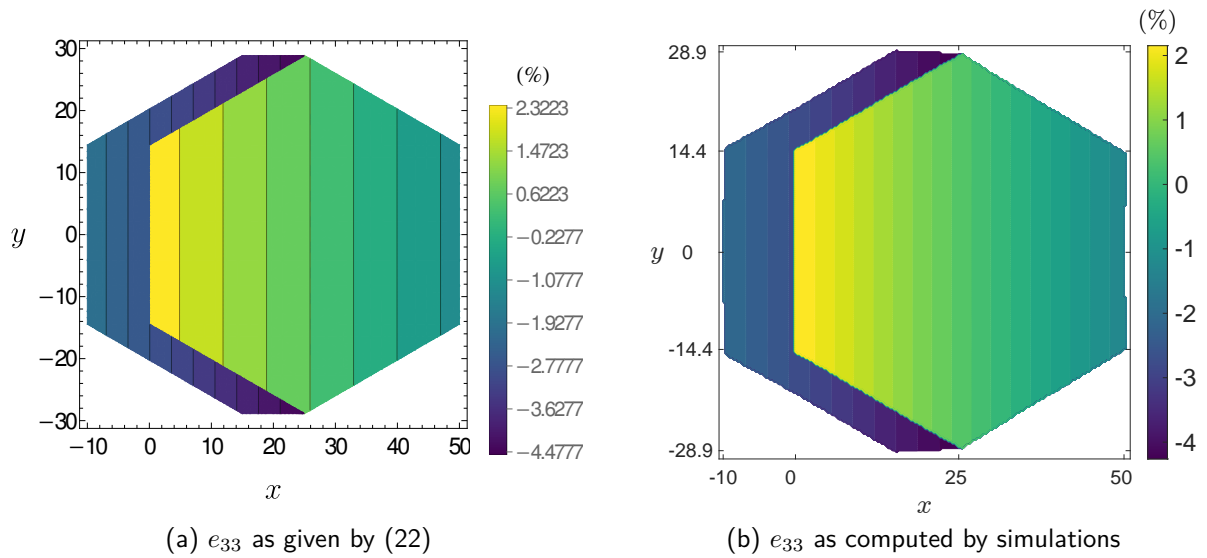


Figure 6: Axial elastic strain component  $e_{33}$  (in %) for a ZB-111 GaAs/In<sub>0.75</sub>Al<sub>0.25</sub>As nanowire with  $d = 50/\sqrt{3}$  nm and  $\delta = 10$  nm. *Left panel:* Analytical strain computed via (22) in the reference configuration. *Right panel:* Numerical strain in the deformed space.

influence on the electrical and optoelectronic characteristics [6] of the nanostructure. Understanding the prevalence of these components allows for the targeted engineering of strain in nanowire devices, opening up new possibilities for designing and optimizing their performance.

### 5.3 Comparison between analytical and simulated curvatures

Next, we compare the theoretical formula for the curvature stated in (21) with the computed curvature after running the 3D FEM simulation and then numerically estimating the curvature.

Figure 8a compares the curvature formula (solid lines) and simulated curvature (dots) for various hexagonal core sides  $d$  and stressor thicknesses  $\delta$ . We use a ZB-(111) nanowire which consists of a GaAs core and a In<sub>0.75</sub>Al<sub>0.25</sub>As stressor with material parameters stated in Table 1. The meaning of these parameters are explained visually in Figure 2a. Both curvatures are varied with respect to the shell thickness  $\delta$ . The four different colors represent four different hexagonal core sides  $d = w/\sqrt{3}$ , with  $w = 30$  (blue),  $w = 45$  (gold),  $w = 50$  (red), and  $w = 60$  (green). For the simulation we use between 188,640 to 293,760 cubic finite elements. The figure shows very good agreement for all 16 different shell thicknesses and core sizes, thus validating our numerical implementation of the nanowire model through analytical theory.

Figure 8b shows the curvature with respect to the lattice mismatch  $l_m$  for two bimetallic beams; one with equal core and shell regions ( $h_1 = h_2 = 25$  nm) and  $w = 50$  nm, and the other with heights  $h_1 = 37.5$  nm,  $h_2 = 12.5$  nm, and width  $w = 100$  nm. In the first case, the core and shell regions are made up of the same isotropic ZB-001 material. As a result, the curvature remains unaffected by the strain-stress parameters of each material since their Young's moduli are identical. For the second beam we use a generic (anisotropic) ZB-001 GaAs/In<sub>0.25</sub>Al<sub>0.75</sub>As core/shell composition. In both tests the lattice constants of the materials do not correspond to the physical values; instead the lattice constants are adjusted as described in Section 5.1. The 3D simulations of the curvature agree well with the curvature equation (24).

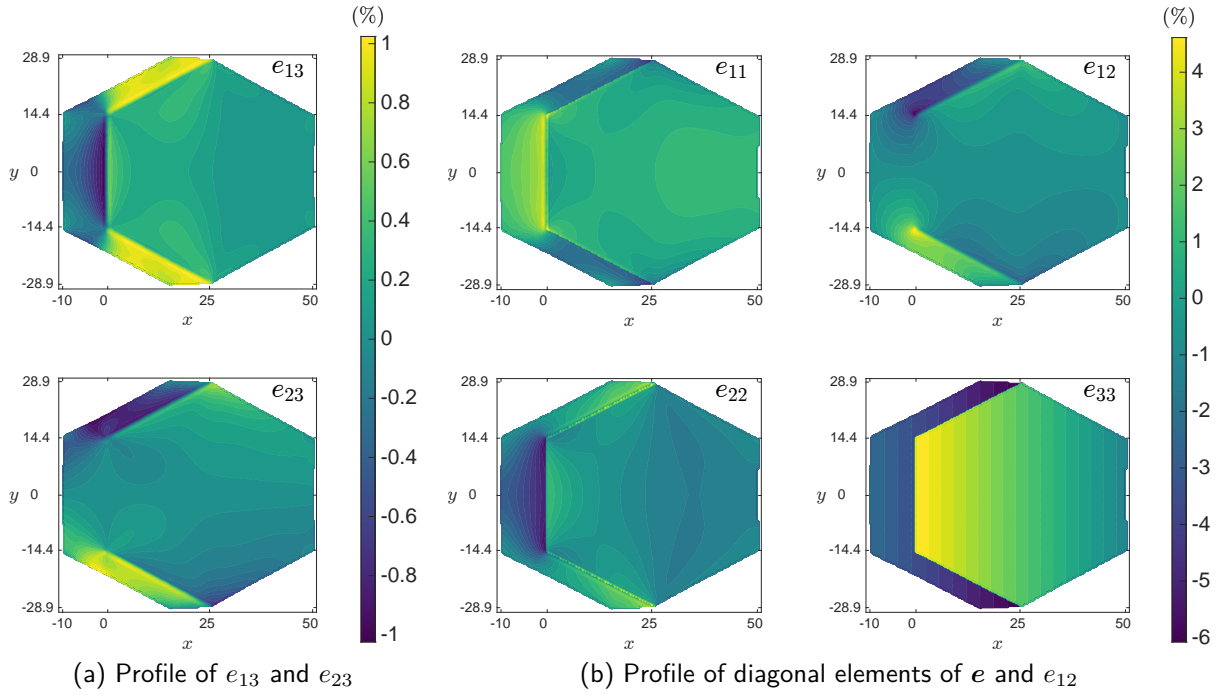


Figure 7: Elastic strain distribution on a mid-length cross section of a 2000 nm long ZB-(111) GaAs/In<sub>0.75</sub>Al<sub>0.25</sub>As core/stressor nanowire. The left panel shows two off-diagonal elastic strain components and the right panel depicts the diagonal and  $e_{12}$  entries. The diagonal and the  $e_{12}$  components are about four times larger in absolute value than the remaining two off-diagonal components, and hence they have a bigger impact on the electrical and optoelectronic properties of the nanostructure.

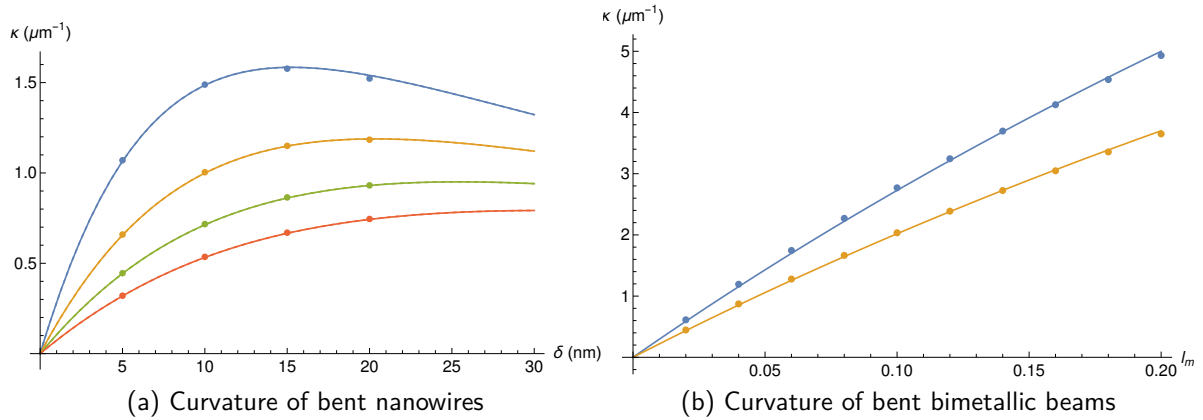


Figure 8: *Left panel:* Curvature of a bent GaAs/In<sub>0.5</sub>Al<sub>0.5</sub>As nanowires with respect to stressor thickness  $\delta$ . The core of the nanowire has hexagon sides  $d = w/\sqrt{3}$  with  $w \in \{30, 45, 50, 60\}$  nm (blue, gold, red, and green curves respectively). The solid lines correspond to the curvature formula (21) and the dots to simulation data. *Right panel:* Calculated and theoretical curvature with respect to the lattice mismatch of bent bimetallic beams with different cross sections. The solid line corresponds to the curvature equation (24) and the dots markers to simulation values. We use beams with  $h_1 = h_2 = 25$  nm and  $w = 50$  nm (blue), and  $h_1 = 37.5$  nm,  $h_2 = 12.5$  nm, and  $w = 100$  nm (gold).

## 6 Conclusion

In conclusion, we proposed a constitutive model for nonlinear elastic heterostructures such as bimetallic beams or nanowires that takes into account local prestrain within each distinct material region. We solve the model via FEM simulations. To assess the quality of our numerical solutions we derived two different analytical expressions for the curvatures of heterostructures due to lattice mismatch between the different material regions. We find excellent agreement between the analytical expressions with our simulated curvature.

Our investigation into the strain distribution within the ZB-(111) GaAs/ $\text{In}_x\text{Al}_{1-x}\text{As}$  nanowire reveals that the diagonal and  $e_{xy}$  components significantly outweigh the other two off-diagonal components in magnitude. This finding underscores the pivotal role of axial and at least one shear strain component in shaping the electrical and optoelectronic properties of nanowire structures, offering valuable insights for the design and optimization of future nanowire-based devices.

## A Energy function derivative

Let the stored energy function given by (13) where  $e_{ij} = \frac{1}{2} (M_{is}^{-\text{T}} F_{sp}^{\text{T}} F_{ps'} M_{s'j}^{-1} - \delta_{ij})$ ,  $s$  and  $s'$  are dummy indices of matrix-matrix multiplication, and  $\delta_{ij}$  is the Kronecker delta. The partial derivative of  $e_{ij}$  with respect to an arbitrary element of  $\mathbf{F}$  is (using the fact that  $M_{is}^{-\text{T}} = M_{si}^{-1}$ )

$$\begin{aligned} \frac{\partial e_{ij}}{\partial F_{mn}} &= \frac{1}{2} (M_{si}^{-1} \delta_{pm} \delta_{sn} F_{ps'} M_{s'j}^{-1} + M_{si}^{-1} F_{ps} \delta_{pm} \delta_{s'n} M_{s'j}^{-1}) \\ &= \frac{1}{2} (F_{ms'} M_{s'j}^{-1} M_{in}^{-\text{T}} + F_{ms} M_{si}^{-1} M_{jn}^{-\text{T}}). \end{aligned}$$

Since  $e$  is symmetric, then  $e_{ij} = e_{ji}$  and

$$\frac{\partial e_{ij}}{\partial F_{mn}} = F_{ms} M_{si}^{-1} M_{jn}^{-\text{T}}.$$

Plugging the above into the partial derivative of (13) with respect to  $F_{mn}$ , yields

$$\begin{aligned} \frac{\partial W}{\partial F_{mn}} &= \frac{1}{2} \det(\mathbf{M}) \mathbf{C}_{ijkl} \left( \frac{\partial e_{ij}}{\partial F_{mn}} e_{kl} + e_{ij} \frac{\partial e_{kl}}{\partial F_{mn}} \right) \\ &= \frac{1}{2} \det(\mathbf{M}) (F_{ms} M_{si}^{-1} \mathbf{C}_{ijkl} e_{kl} M_{jn}^{-\text{T}} + F_{ms} M_{sk}^{-1} \mathbf{C}_{ijkl} e_{ij} M_{ln}^{-\text{T}}) \\ &= \det(\mathbf{M}) (F_{ms} M_{si}^{-1} \mathbf{C}_{ijkl} e_{kl} M_{jn}^{-\text{T}}) \\ &= \det(\mathbf{M}) M_{mi}^{-1} [\mathbf{C} : \mathbf{e}]_{ij} M_{jn}^{-\text{T}} \\ &= \det(\mathbf{M}) [\mathbf{F} \mathbf{M}^{-1} (\mathbf{C} : \mathbf{e}) \mathbf{M}^{-\text{T}}]_{mn}, \end{aligned}$$

where  $[\cdot]_{ij}$  denotes the  $ij$ -element of a matrix. We also used the symmetry properties of tensor  $\mathbf{C}$ , namely  $\mathbf{C}_{ijkl} = \mathbf{C}_{jikl} = \mathbf{C}_{ijlk} = \mathbf{C}_{klij}$ . Therefore,

$$\frac{\partial W}{\partial \mathbf{F}} = \det(\mathbf{M}) \mathbf{F} \mathbf{M}^{-1} (\mathbf{C} : \mathbf{e}) \mathbf{M}^{-\text{T}}.$$

## B Discretisation by Finite Element Methods

This section gives some details on the employed discretization via classical finite element methods and our implementation of the Newton iteration and a modification to improve its convergence.

### B.1 Weak formulation and discretization

For two arbitrary tensors  $\mathbf{A}(\mathbf{x})$  and  $\mathbf{B}(\mathbf{x})$  in  $\mathbb{R}^{3 \times 3}$  we define the inner product in  $L^2(\omega)$  for some subdomain  $\omega \subseteq \Omega$  by

$$(\mathbf{A}, \mathbf{B})_{L^2(\omega)} := \int_{\omega} \langle \mathbf{A}(\mathbf{x}), \mathbf{B}(\mathbf{x}) \rangle_{\mathbb{F}} \, d\mathbf{x},$$

where  $\langle \cdot, \cdot \rangle_{\mathbb{F}}$  is the Frobenius inner product.

The weak formulation of (14) is obtained by testing with (smooth) test functions  $\mathbf{v}(\mathbf{x}) \in V \subseteq \mathbb{R}^3$ , and applying integration by parts, i.e.,

$$(-\operatorname{div} g(\nabla \mathbf{u}), \mathbf{v})_{L^2(\Omega)} = (g(\nabla \mathbf{u}), \nabla \mathbf{v})_{L^2(\Omega)} =: \alpha(\mathbf{u}, \mathbf{v}) \quad \text{for all } \mathbf{v} \in V.$$

Here,  $g : \mathbb{R}^{3 \times 3} \rightarrow \mathbb{R}^{3 \times 3}$  abbreviates the nonlinear expression

$$g(\mathbf{A}) := \left( \det(\mathbf{M})(\mathbf{I} + \mathbf{A})\mathbf{M}^{-1}\mathbf{S}(\mathbf{A})\mathbf{M}^{-T} \right)$$

and  $\mathbf{S}$  refers to the strain as defined in (5), but in the more abstract form

$$\mathbf{S}(\mathbf{A}) = \mathbf{C} : \frac{1}{2}(\mathbf{A} + \mathbf{A}^T + \mathbf{A}^T \mathbf{A}).$$

For some regular triangulation  $\mathcal{T}$  let  $V_h \subseteq \mathbb{R}^3$  denote some conforming finite element ansatz space. Then, the discrete weak problem seeks a function  $\mathbf{u}_h \in V_h$ , such that

$$\alpha(\mathbf{u}_h, \mathbf{v}_h) = 0 \quad \text{for all } \mathbf{v}_h \in V_h.$$

Choosing a finite element basis  $\{\varphi_j\}_{j=1, \dots, N}$  for  $V_h$  where  $N$  is the dimension of  $V_h$ , we can express the discrete functions as linear combinations, i.e.,  $\mathbf{u}_h(\mathbf{y}) := \sum_{j=1}^N y_j \varphi_j$ , with  $\mathbf{y} = (y_j) \in \mathbb{R}^N$ . The discrete problem of (14) seeks a coefficient vector  $\mathbf{y} \in \mathbb{R}^N$  such that

$$\mathbf{G}(\mathbf{y}) = \mathbf{0} \text{ for all } \mathbf{y} \in \mathbb{R}^N \iff G_j(\mathbf{y}) = 0 \text{ for all } \varphi_j \in V_h, \quad (25)$$

where  $\mathbf{G} : \mathbb{R}^N \rightarrow \mathbb{R}^N$  is a nonlinear function  $\mathbf{G} = (G_1, \dots, G_N)$  defined by

$$G_j(\mathbf{y}) := a(\mathbf{u}_h(\mathbf{y}), \varphi_j) = \sum_{T \in \mathcal{T}} (g(\nabla \mathbf{u}_h(\mathbf{y})|_T), \nabla \varphi_j)_{L^2(T)}$$

## B.2 Newton's method

In order to solve the nonlinear system (25) a Newton iteration can be employed. Given an iterate  $\mathbf{y}_{n-1}$ , Newton's method suggests that the next iterate  $\mathbf{y}_n$  should be calculated by

$$\mathbf{y}_n = \mathbf{y}_{n-1} - (D\mathbf{G}(\mathbf{y}_{n-1}))^{-1} \mathbf{G}(\mathbf{y}_{n-1}). \quad (26)$$

The evaluation of function  $G_j$  employs a quadrature rule on every cell  $T \in \mathcal{T}$  with quadrature points  $x_{qp,T}$  and quadrature weights  $w_{qp}$  such that

$$G_j(\mathbf{y}) = \sum_{T \in \mathcal{T}} (g(\nabla \mathbf{u}_h(\mathbf{y})|_T), \nabla \varphi_j)_{L^2(T)} = \sum_{T \in \mathcal{T}} \sum_{x_{qp}} w_{qp} \langle g(\nabla \mathbf{u}_h(x_{qp,T}; \mathbf{y})), \nabla \varphi_j(x_{qp}) \rangle_{\mathbb{F}}.$$

Since, the integrand is a polynomial, a quadrature rule can be chosen that allows an exact integration. Eventually, the global Jacobian  $D\mathbf{G}(\mathbf{y})$  can be computed by a chain rule from the local Jacobians  $Dg$  of  $g$  and  $\partial(\nabla \mathbf{u}_h)/\partial y_i = \nabla \varphi_i$ . This results in

$$(D\mathbf{G})_{ij} = \partial G_j / \partial y_i = \sum_{T \in \mathcal{T}} \sum_{x_{qp}} w_{qp} \left\langle \left( Dg(\mathbf{u}_h(x_{qp,T}; \mathbf{y})) \nabla \varphi_i(x_{qp}) \right), \nabla \varphi_j^\top(x_{qp}) \right\rangle_{\mathbb{F}}.$$

In our Julia implementation, the local Jacobians of the kernel function  $g$  are computed by automatic differentiation.

According to (26) the new iterate  $\mathbf{y}_n$  can be found by solving the linear system of equations

$$D\mathbf{G}(\mathbf{y}_{n-1})\mathbf{y}_n = D\mathbf{G}(\mathbf{y}_{n-1})\mathbf{y}_{n-1} - \mathbf{G}(\mathbf{y}_{n-1})$$

Depending on the strength of the nonlinearity and the initial configuration, Newton's method may not converge as described. To improve the convergence of the Newton method, we employ a kind of homotopy approach where we scale the most severe nonlinearity by a some factor  $\beta$  and use the inner kernel function

$$g(\mathbf{A}) := \det(\mathbf{M})(\mathbf{I} + \beta \mathbf{A})\mathbf{M}^{-1} \mathbf{S}(\mathbf{A})\mathbf{M}^{-T}.$$

This means we first solve the problem for  $\beta = 0$  and use this solution as an initial value for the next homotopy embedding iteration with a larger  $\beta$  and so on, until we arrive at the final solution for  $\beta = 1$ . In our simulations we used 5 homotopy iterations.

## B.3 Meshes

Figure 9 shows two exemplary meshes for the bimetallic beam's and the nanowire's cross sections used in the simulations. In both cases, the interface where the stressor and core meet is resolved with a finer mesh. To reduce the computation cost, we introduced within the core region another hexagon inside which a coarser mesh is used, see Figure 9a.

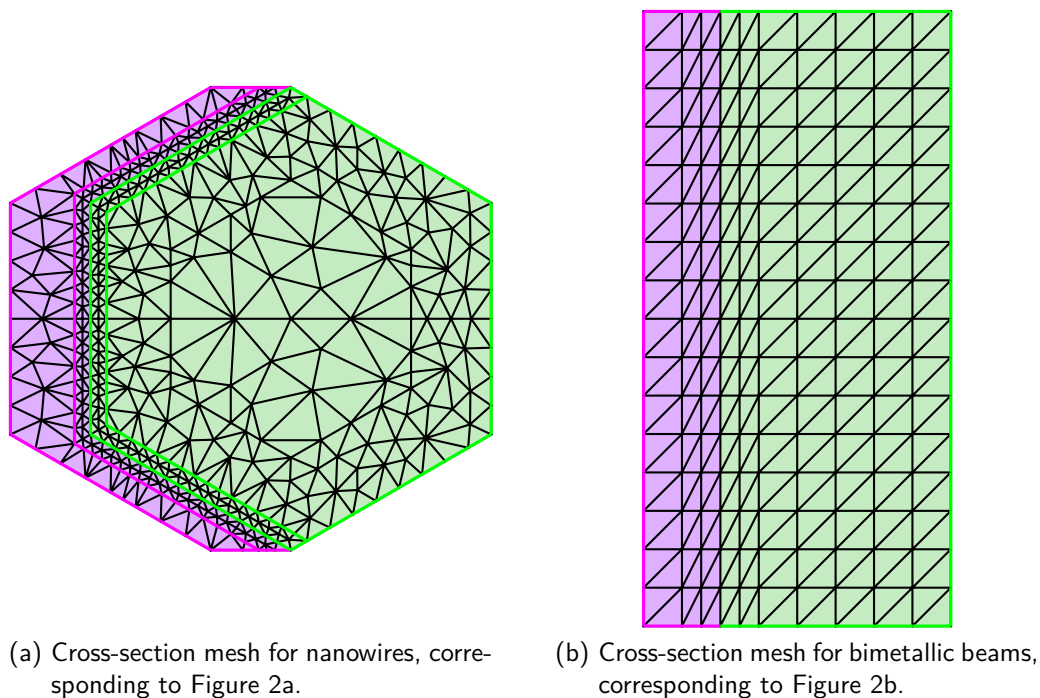


Figure 9: Exemplary finite element meshes used in the simulations.

## References

- [1] ARRUDA, E. M., AND BOYCE, M. C. A three-dimensional constitutive model for the large stretch behavior of rubber elastic materials. *Journal of the Mechanics and Physics of Solids* 41, 2 (1993), 389–412.
- [2] BAUER, R., NEUKAMM, S., AND SCHÄFFNER, M. Derivation of a homogenized bending–torsion theory for rods with micro-heterogeneous prestrain. *Journal of Elasticity* 141, 1 (2020), 109–145.
- [3] BOXBERG, F., SØNDERGAARD, N., AND XU, H. Elastic and piezoelectric properties of zincblende and wurtzite crystalline nanowire heterostructures. *Advanced materials* 24, 34 (2012), 4692–4706.
- [4] CIARLET, P. G. *Mathematical elasticity. Vol. I*, vol. 20 of *Studies in Mathematics and its Applications*. North-Holland Publishing Co., Amsterdam, 1988. Three-dimensional elasticity.
- [5] DENEKE, C., MÜLLER, C., JIN-PHILLIPP, N. Y., AND SCHMIDT, O. G. Diameter scalability of rolled-up In(Ga)As/GaAs nanotubes. *Semiconductor Science and Technology* 17, 12 (2002), 1278.
- [6] FARRELL, P., KAYSER, S., AND ROTUNDO, N. Modeling and simulation of the lateral photovoltage scanning method. *Computer and Mathematics with Applications* 102 (2021), 248–260.
- [7] FARRELL, P., ROTUNDO, N., DOAN, D. H., KANTNER, M., FUHRMANN, J., AND KOPRUCKI, T. Mathematical methods: Drift-diffusion models. In *Handbook of*

- Optoelectronic Device Modeling and Simulation*, vol. 2. CRC Press, 2017, ch. 50, pp. 733–771. WIAS preprint 2263.
- [8] GANCZARSKI, A. W., EGNER, H., AND SKRZYPEK, J. J. Introduction to mechanics of anisotropic materials. In *Mechanics of Anisotropic Materials*. Springer International Publishing, Cham, 2015, pp. 1–56.
- [9] HOSODA, M., KISHIMOTO, Y., SATO, M., NASHIMA, S., KUBOTA, K., SARAVANAN, S., VACCARO, P. O., AIDA, T., AND OHTANI, N. Quantum-well microtube constructed from a freestanding thin quantum-well layer. *Applied Physics Letters* 83, 5 (2003), 1017–1019.
- [10] HUANG, M., NAIRN, J. A., LIU, F., AND LAGALLY, M. G. Mechanical stability of ultrathin Ge/Si film on SiO<sub>2</sub>: The effect of Si/SiO<sub>2</sub> interface. *Journal of Applied Physics* 97, 11 (2005), 116108.
- [11] KARNAUSHENKO, D., KANG, T., AND SCHMIDT, O. G. Shapeable material technologies for 3d self-assembly of mesoscale electronics. *Advanced Materials Technologies* 4, 4 (2019), 1800692.
- [12] KOHN, R. V., AND O'BRIEN, E. On the bending and twisting of rods with misfit. *Journal of Elasticity* 130 (2018), 115–143.
- [13] LEKHNITSKII, S. *Mechanics of anisotropic materials*. Mir Publishers, 1981. in Russian: Nauka 1977.
- [14] LEWIS, R. B., CORFDIR, P., KÜPERS, H., FLISSIKOWSKI, T., BRANDT, O., AND GEELHAAR, L. Nanowires bending over backward from strain partitioning in asymmetric core-shell heterostructures. *Nano Letters* 18 (2018), 2343–2350.
- [15] LIU, F., HUANG, M., RUGHEIMER, P. P., SAVAGE, D. E., AND LAGALLY, M. G. Nanostressors and the nanomechanical response of a thin silicon film on an insulator. *Physical Review Letters* 89 (2002), 136101.
- [16] MARTIN, R. M. Piezoelectricity. *Physical Review B* 5 (1972), 1607–1613.
- [17] MCDERMOTT, S., AND LEWIS, R. B. Bending of GaAs-InP core-shell nanowires by asymmetric shell deposition: implications for sensors. *ACS Applied Nano Materials* 4, 10 (2021), 10164–10172.
- [18] MERDON, C., AND FUHRMANN, J. chmerdon/gradientrobustmultiphysics.jl: v0.11.3, 2023.
- [19] MILLER, W. H. *A treatise on crystallography*. Cambridge: Pitt Press, 1839.
- [20] NESPOLO, M. The ash heap of crystallography: restoring forgotten basic knowledge. *Journal of Applied Crystallography* 48, 4 (2015), 1290–1298.
- [21] OGDEN, R. W. Large deformation isotropic elasticity—on the correlation of theory and experiment for incompressible rubberlike solids. *Proceedings of the Royal Society of London. Series A, Mathematical and Physical Sciences* 326, 1567 (1972), 565–584.

- [22] SADIK, S., AND YAVARI, A. On the origins of the idea of the multiplicative decomposition of the deformation gradient. *Mathematics and Mechanics of Solids* 22, 4 (2017), 771–772.
- [23] SARNEY, W. L. Hexagonal close-packed (hcp) crystallography, diffraction, and indexing conventions. Tech. rep., 2020.
- [24] SCHMIDT, O. G., AND EBERL, K. Thin solid films roll up into nanotubes. *Nature* 410, 6825 (2001), 168–168.
- [25] SCHULZ, S., CARO, M., O'REILLY, E., AND MARQUARDT, O. Symmetry-adapted calculations of strain and polarization fields in (111)-oriented zinc-blende quantum dots. *Physical Review B* 84 (2011), 125312.
- [26] SONGMUANG, R., DENEKE, C., AND SCHMIDT, O. G. Rolled-up micro- and nanotubes from single-material thin films. *Applied Physics Letters* 89, 22 (2006), 223109.
- [27] TIMOSHENKO, S. Analysis of bi-metal thermostats. *Journal of the Optical Society of America* 11, 3 (1925), 233–255.
- [28] TRELOAR, L. R. G. The elasticity of a network of long-chain molecules—ii. *Transactions of the Faraday Society* 39 (1943), 241–246.
- [29] TRUESDELL, C., AND TOUPIN, R. The classical field theories. In *Principles of Classical Mechanics and Field Theory*. Springer Berlin Heidelberg, Berlin, Heidelberg, 1960, pp. 226–858.
- [30] TRUESDELL, C., AND WALTER, N. *The Non-Linear Field Theories of Mechanics*. Springer Berlin Heidelberg, Berlin, Heidelberg, 2004.
- [31] VURGAFTMAN, I., MEYER, J. R., AND RAM-MOHAN, L. R. Band parameters for iii–v compound semiconductors and their alloys. *Journal of Applied Physics* 89, 11 (2001), 5815–5875.
- [32] YUDIN, P. V., AND TAGANTSEV, A. K. Fundamentals of flexoelectricity in solids. *Nanotechnology* 24, 43 (2013), 432001.
- [33] ZANG, J., AND LIU, F. Modified timoshenko formula for bending of ultrathin strained bilayer films. *Applied Physics Letters* 92, 2 (2008), 021905.
- [34] ZUBKO, P., CATALAN, G., AND TAGANTSEV, A. K. Flexoelectric effect in solids. *Annual Review of Materials Research* 43, 1 (2013), 387–421.